HHS Public Access

Author manuscript

Nat Commun. Author manuscript; available in PMC 2012 December 20.

Published in final edited form as:

Nat Commun. 2012 ; 3: 1193. doi:10.1038/ncomms2197.

Self-luminescing BRET-FRET near infrared dots for in vivo lymph node mapping and tumor imaging

Liqin Xiong[1], **Adam J. Shuhendler**, and **Jianghong Rao**[*]

Molecular Imaging Program at Stanford (MIPS), Departments of Radiology and Chemistry, Stanford University, Stanford, CA 94305-5484, USA Tel: 1-650-736-8563 Fax: 1-650-736-7925

Abstract

Strong autofluorescence from living tissues, and the scattering and absorption of short-wavelength light in living tissues, significantly reduce sensitivity of *in vivo* fluorescence imaging. These issues can tackled by using imaging probes that emit in the near-infrared (NIR) wavelength range. Here we describe self-luminescing NIR-emitting nanoparticles employing an energy transfer relay that integrates bioluminescence resonance energy transfer (BRET) and fluorescence resonance energy transfer (FRET), enabling *in vivo* NIR imaging without external light excitation. Nanoparticles were 30-40 nm in diameter, contained no toxic metals, exhibited long circulation time and high serum stability, and produced strong NIR emission. Using these nanoparticles, we successfully imaged lymphatic networks and vasculature of xenografted tumors in living mice. The self-luminescing feature provided excellent tumor-to-background ratio (>100) for imaging very small tumors (2-3 mm in diameter). Our results demonstrate that these new nanoparticles are well suited to *in vivo* imaging applications such as lymph node mapping and cancer imaging.

Introduction

Fluorescence imaging has become a powerful technique to visualize biology in its native physiological settings in a living subject[1-4], and has been used even in clinics for guiding surgery in cancer patients[5]. One major obstacle encountered with fluorescence imaging is strong autofluorescence arising from living tissues[6] that significantly compromises imaging sensitivity and specificity. Addressing this technical challenge demands the development of imaging probes that can emit in the near-infrared (NIR) wavelength range where autofluorescence background is significantly decreased, a spectral window where

[*] To whom correspondence should be addressed: jrao@stanford.edu.

[1]Present address: School of Biomedical Engineering, Shanghai Jiao Tong University, Shanghai 200030, China

Author Contributions

L.X. and J.R. conceived of the nanoparticle design, L.X. prepared and characterized the nanoparticles, and performed *in vivo* studies and analyzed the data. A.J.S. and J.R. conceived of the gel phantom and imaging penetration depth studies, and A.J.S. and L.X. performed the imaging depth studies and analyzed the data. L.X., J.R., and A.J.S. wrote the manuscript.

Competing Financial Interests

Stanford University is filing patent protection on some of the results in this manuscript on behalf of L.X. and J.R. The provisional patent application number is 61/623,224.

Supplementary Information

Supplementary information consists of 15 figures, supplementary methods, and associated references.

nanoparticle probes offer great potential. One such example are QD-BRET probes based on bioluminescence resonance energy transfer (BRET) between quantum dots (QD) and a bioluminescent protein *R. reniformis* luciferase (QD-BRET)[7,8]. QD-BRET has been applied to *in vitro* detection[9-11], protease and nucleic acid sensing[12-14], and *in vivo* lymphatic imaging[15]. However, unfavorable *in vivo* pharmacokinetics of QDs after systemic injection, concerns regarding their *in vivo* stability and the intrinsic toxicity of heavy metals of the QD nanoparticles have largely limited their applications in translational research[16-18].

In this work, we report the development of new self-luminescing NIR nanoparticles for imaging living mice by integrating BRET and FRET in an energy transfer relay to enable self-luminescing NIR emission. We applied these new nanoparticles to image lymphatic networks of mice and found highly efficient labeling of lymph nodes. Using cyclic RGD peptides as the targeting ligand, we demonstrated their high sensitivity for targeted tumor imaging in living mice: a tumor-to-background ratio of over 100 in comparison to a ratio of just 3 to 6 with fluorescence imaging. The self-luminescing NIR NPs offer a more efficient strategy for lymph node mapping and cancer imaging by combining NIR bioluminescence for *in vivo* imaging and fluorescence for *ex vivo* imaging.

Results

Preparation of BRET-FRET NIR Nanoparticles

As outlined in **Figure 1**, a dual resonance energy transfer relay process was used to design self-luminescing NIR nanoparticles by combining BRET and FRET. Semiconductor polymer nanoparticles with poly[2-methoxy-5-((2-ethylhexyl)oxy)-*p*-phenylenevinylene] (MEH-PPV) as the matrix were used because of their generally low or no toxicity, bright fluorescence intensity, and excellent photostability[19-24]. MEH-PPV NPs absorb maximally at 503 nm (**Fig. 2a**). Luc8 (an eight-mutation variant of *R. reniformis* luciferase) emits blue light with a peak at 480 nm upon addition of its substrate coelenterazine[25]. The good overlap between the MEH-PPV absorption and Luc8 emission suggests that efficient BRET can occur and generate self-luminescing polymeric nanoparticles.

To shift the luminescent emission of the nanoparticles to longer wavelengths for *in vivo* imaging, we doped the polymer matrix with NIR fluorescent dyes such as NIR775 (**Fig. 1**). Following BRET from Luc8 to the polymer matrix, FRET could occur between the polymer matrix and the doped NIR fluorophore (**Fig. 2a, b**). This BRET-FRET relay process produces self-luminescing BRET-FRET NIR nanoparticles (abbreviated as **RET$_2$IR**).

Polymer nanoparticles are generally hydrophobic and not water soluble, limiting their biological applications. An amphiphilic polymer, PS-PEG-COOH, was introduced to coat the nanoparticles with a biocompatible shell, orienting its hydrophobic portion within the hydrophobic core of the polymer matrix and exposing its hydrophilic groups on the nanoparticle surface (**Fig. 1**). This PEG coating can greatly improve the water solubility and biocompatibility of the nanoparticles, and also help reduce serum protein adsorption and suppress immune reactions, thereby increasing the blood circulation time of the nanoparticles *in vivo*. The carboxlyate groups presented at the PEG termini are available for bioconjugation of Luc8 and tumor-targeting ligands.

RGD (arginine-glycine-aspartic) peptides have a strong affinity for the cell adhesion receptor integrin $\alpha_v\beta_3$, which plays a pivotal role in tumor angiogenesis, and have been used for *in vivo* imaging of a variety of cancers[26-29]. We conjugated cyclic RGD peptides (cRGD) via their amino groups to the PS-PEG-COOH coated **RET$_2$IR** (**Fig. 1**) for imaging human glioblastoma U87MG tumor xenografts in nude mice.

We first synthesized the MEH-PPV@NIR@PEG nanoparticles (abbreviated as **RET$_1$IR** since there was just FRET in this nanoparticle) using a nanoprecipitation method[30]. To minimize the self-quenching effect among encapsulated NIR dyes, the optimal ratio of NIR775 to the MEH-PPV matrix (by weight) was found to be 0.004-0.02 (**Supplementary Figure S1**). Luc8 was conjugated with carbodiimide chemistry between the carboxylate groups on the nanoparticles and the free amino groups on Luc8. The number of Luc8 on each nanoparticle was estimated to be 5.3 on average (**Supplementary Figure S2**). The synthesized **RET$_2$IR** NPs were stable in PBS with no aggregation observed after storage at 4°C at a concentration of 150 μg/mL for weeks.

Characterization of RETIR Nanoparticles

The **RET$_2$IR** NPs exhibited a broad UV/Vis band with a maximum at 503 nm. Under excitation at 490 nm, they exhibited very weak MEH-PPV emission at 594 nm but a strong NIR peak at 778 nm (**Fig. 2a**). At a blending ratio of 0.012 (NIR775 / MEH-PPV by weight), the fluorescence quantum yield of the **RET$_2$IR** NPs at 594 nm emission (the polymer matrix) in water dropped from its original value of 0.18 to 0.03 after doping with NIR775, while the quantum yield of the 778 nm emission (NIR775) in water was around 0.09 (in comparison, the quantum yield of free NIR775 in THF was 0.08). This result confirms that FRET occurred efficiently from the MEH-PPV matrix to NIR775 in the **RET$_2$IR** NPs.

We examined the bioluminescence emission of the **RET$_2$IR** NPs upon addition of coelenterazine. In addition to the emission of Luc8 at 480 nm, two new emission peaks at 594 nm (relatively weak, from MEH-PPV matrix) and 778 nm (strongest, from NIR775) were detected (**Fig. 2b**); this is consistent with our design of the BRET-FRET relay process from Luc8 to the polymer matrix and then to NIR775. The overall BRET ratio, determined by dividing the acceptor emission (550-810 nm) by the donor emission (400-550 nm), was 2.5 (corresponding to an efficiency of 71%), which was nearly double that of QDLuc8 nanoparticles that were previously reported to have a BRET ratio of 1.29[7].

Transmission Electron Microscopy (TEM) and Dynamic Light Scattering (DLS) indicated an average particle diameter of approximately 27 nm for the **RET$_1$IR** NPs (**Fig. 2c, d**; **Supplementary Figure S3**). Conjugation to Luc8 and cRGD increased the average hydrodynamic diameter to approximately 33 nm, 38 nm and 41 nm for the cRGD conjugated **RET$_1$IR** (**RET$_1$IR@cRGD**) NPs, **RET$_2$IR** NPs and the cRGD conjugated **RET$_2$IR** (**RET$_2$IR@cRGD**) NPs, respectively (**Fig. 2d**). Gel electrophoresis analysis of these nanoparticles in 0.5% agarose showed a different mobility than the original **RET$_1$IR** NPs due to changes in the surface charge and particle size following bioconjugation (**Fig. 2e**).

We examined the stability of the **RET$_2$IR** NPs in mouse serum by monitoring both their bioluminescence and fluorescence at 37°C for 24 h (**Fig. 2f**). The bioluminescence intensity of nanoparticles remained stable over 24 h and even increased slightly by 10% at 24 h. The fluorescence intensity of the nanoparticles was nearly unchanged with just 3% decrease after 24 h. As expected, the stability of the **RET$_2$IR** NPs in mouse serum was higher at 4°C and 22°C than at 37°C (**Supplementary Figure S4**). In comparison to QDs, the **RET$_2$IR** NPs are more stable in mouse serum and suitable for *in vivo* imaging applications[16]. The circulation time of the **RET$_1$IR** NPs in the blood was long with an estimated half-life of approximately 8 hours (**Fig. 2g**).

The depth of signal penetration of **RET$_2$IR** was assessed both *in vitro* in a tissue phantom (**Supplementary Figure S5**) and *in vivo* in live mice (**Supplementary Figure S6**) in direct comparison to Luc8 and QDLuc8. In the tissue phantom, **RET$_2$IR** luminescence signal was observable even at 2 cm of gel depth at signal intensities significantly greater than QDLuc8, while the signal depth penetration of Luc8 was limited to 1.5 cm (**Supplementary Figure S5**). In live mice, the luminescence signal penetration subcutaneously (**Supplementary Figure S6a and b**) and through the whole animal (**Supplementary Figure S6 c and d**) of **RET$_2$IR** was significantly greater than Luc8, and was equivalent to QDLuc8. In fact an observed advantage of **RET$_2$IR** nanoparticles was the maintained evolution of luminescence signal following the administration of coelenterazine relative to QDLuc8, which exhibited faster signal decay kinetics especially under deeper penetration depths *in vivo* (**Supplementary Figure S7**).

The cytotoxicity of the **RET$_1$IR** NPs was evaluated by the MTT assay in human glioblastoma U87MG cells, and no significant differences in cell viability were observed in the absence or presence of the **RET$_1$IR** NPs at a concentration of 5–200 μg/mL at 37 °C for 24 h (**Fig. 2h**). In conjunction with the imaging depth of penetration studies, this data demonstrates that **RET$_2$IR** nanoparticles are a safer alternative to QDLuc8 as they are free from toxic heavy metals, and that there is no loss of imaging depth penetration performance *in vivo*.

Lymph Node Imaging With RETIR Nanoparticles

At 24 h after tail vein injection of the **RET$_1$IR** NPs into nude mice, the mice were surgically opened for imaging (**Fig. 3a, b**). Strong NIR fluorescence signals were detected in the lymphatic networks: neck lymph nodes (NL), axillary lymph nodes (AX), lateral thoracic lymph nodes (LT), and inguinal lymph nodes (IN) could all be clearly imaged with NIR fluorescence emission. After the removal of internal organs, renal and iliac lymph nodes were also clearly visualized with strong NIR fluorescence (**Supplementary Figure S8**). The lymphatic system is difficult to identify because its channels are small and not directly accessible. Nanoparticles have been evaluated for labeling the AX, IN, or neck lymph nodes[31-36]. Our results show that the **RET$_1$IR** NPs allow highly efficient labeling of all the lymph nodes in the lymphatic networks after tail-vein injection.

Similarly, the **RET$_2$IR** NPs (~2 μg) were introduced into the forepaws of mice via intradermal injections. Within 10 min of injection, the AX could be readily visualized non-

invasively by bioluminescence imaging (**Fig. 3c**). When followed by *in vivo* fluorescence imaging, lower fluorescent signals were obtained at the AX in comparison with bioluminescence imaging (**Fig. 3d**). After **RET$_2$IR** NPs were injected into all four paws (each at ~2 μg), all lymph nodes in the same mouse were clearly visualized by bioluminescence imaging (**Fig. 3e**). The axillary and popliteal lymph nodes were still clearly labeled even 10 days later (**Supplementary Figure S9**).

Tumor Imaging With RET$_1$IR Nanoparticles

To evaluate **RET$_2$IR** NPs for cancer imaging, we first tested the cRGD conjugated **RET$_1$IR** (**RET$_1$IR@cRGD**) NPs for imaging $\alpha_v\beta_3$ of human glioblastoma U87MG cells in culture, which express high levels of $\alpha_v\beta_3$. After 2.5 h incubation, intense NIR fluorescence was detected at the cell membrane and in the cytoplasm (**Fig. 4a**), of which the cytoplasmic signal increased with time up to 24 h (**Fig. 4b**). DAPI staining revealed little NIR fluorescence signal in the nucleus (**Supplementary Figure S10**). In contrast, the control **RET$_1$IR** NPs without cRGD resulted very weak NIR fluorescence from U87MG cells under the same experimental conditions (**Fig. 4c**).

The **RET$_1$IR@cRGD** NPs were then injected intravenously into nude mice bearing a U87MG tumor on the left shoulder (~50 μg per animal), and the mice were imaged at multiple time points postinjection (**Fig. 4d**). The *in vivo* fluorescence spectrum of the **RET$_1$IR@cRGD** NPs was collected from 520 nm to 840 nm with a bandwidth of 20 nm and an excitation of 465 nm (**Fig. 4f**). As early as 5 min postinjection, enhanced NIR fluorescence signal (780 nm) was observed in the U87MG tumor (**Fig. 4d**), and gradually increased over time. ROI measurements showed that the NIR fluorescence signal ratio between the tumor and the surrounding tissue was 2.4±0.6 (5 min), 3.3±0.7 (2 h), 6.1±0.2 (24 h) and 5.9±0.6 (48 h) (**Fig. 4g**). There was significant fluorescence signal from the skin after 2 h, which complicated the detection of small size tumors, however the NIR fluorescence signal became stronger when the tumor size became larger, for example, at 8 mm in diameter (**Supplementary Figure S11**). In comparison, no significant NIR fluorescence signal was observed in the tumors injected with the non-targeting **RET$_1$IR** NPs (**Fig. 4e**), and the NIR fluorescence signal ratio between the tumor and background was 2.7, 2.2, 2.9 and 2.1 at 5 min, 2 h, 24 h and 48 h, respectively (**Fig. 4g**). The small increase in the NIR fluorescence signal also observed with the non-targeting **RET$_1$IR** NPs is likely due to the enhanced permeability and retention (EPR) effect.

Fluorescence imaging of sacrificed mice 48 h after injection of **RET$_1$IR@cRGD** NPs revealed uptake in the lymph nodes, skin, stomach, bone, liver, spleen and tumor (**Supplementary Figure S12a, b**). NIR fluorescence signal was also observed in collected urine (**Fig. 4h**), suggesting that **RET$_1$IR** NPs were cleared from the body through the renal system in addition to the hepatobiliary system.

Tumor Imaging With RET$_2$IR Nanoparticles

The **RET$_2$IR** NPs can emit NIR light in the presence of the substrate of Luc8, coelenterazine, without external excitation, and therefore can provide further advantages in comparison to the **RET$_1$IR** NPs. The cRGD conjugated **RET$_2$IR@cRGD** NPs were

similarly evaluated in the U87MG tumor xenograft mouse model. After tail vein injection of the **RET$_2$IR@cRGD** NPs, mice were image serially by bioluminescence imaging. At 5 minutes post injection, strong bioluminescence emission was observed in the U87MG tumor with little signal from other tissues (**Fig. 5a**). The bioluminescence signal ratio between the tumor and background was estimated from ROI measurements to be 66.0±4.8 (5 min), 116.4±7.6 (2 h), 23.3±16.2 (24 h) and 12.9 (48 h) (**Fig. 5c**). The bioluminescence signal from the U87MG tumor decreased significantly when free cRGD (300 μg) was co-injected intravenously with the **RET$_2$IR@cRGD** NPs (**Supplementary Figure S13**), confirming the specific binding of **RET$_2$IR@cRGD** NPs to $\alpha_v\beta_3$ integrin expressed at the neovascular endothelium of the U87MG tumor.

The **RET$_2$IR** NPs allow simultaneous fluorescence and bioluminescence imaging in the same mouse, therefore fluorescence spectral imaging was conducted for comparison. Intense NIR fluorescence signal was observed in the liver, and the NIR fluorescence signal in the tumor was much weaker than the bioluminescence signal (**Fig. 5b**). The fluorescence signal ratio between the tumor and surrounding tissues was 3.4±2.4, 2.4±1.7, 1.3±0.6, and 0.9 at 5 min, 2 h, 24 h and 48 h, respectively (**Fig. 5c**). These results demonstrate that bioluminescence imaging provided much higher sensitivity than fluorescence imaging of tumors *in vivo*.

We further tested the efficiency of the **RET$_2$IR** NPs in imaging smaller tumors (tumor size of 2-3 mm in diameter) (**Fig. 5d & Supplementary Figure S14**). A strong bioluminescence signal was still observed in the U87MG tumor of the mice at 5 min and 2 h. In comparison, the fluorescence signal in the U87MG tumor was much weaker. These results further demonstrated that bioluminescence showed higher sensitivity than fluorescence in cancer imaging *in vivo*.

In vivo biodistribution of the **RET$_2$IR** NPs was similar to that of the **RET$_1$IR@cRGD** NPs except for increased uptake in the lung, which is to be expected due to the relatively larger size of the **RET$_2$IR** NPs (**Supplementary Figure S15**). Renal clearance also occurred with the **RET$_2$IR** NPs as the NIR fluorescence signal was observed in the urine sample collected at 48 h post injection (**Fig. 5e**).

Tumor tissues were excised for sectioning and immunohistochemical staining to confirm the tumor-specific uptake of the **RET$_2$IR** NPs (**Fig. 5f-i**). Tumor slices were fixed and stained with vascular endothelium-specific CD31 antibodies to mark tumor blood vessels for 1h before imaging under a fluorescence microscope. Strong NIR fluorescence was observed within the tumor tissue (**Fig. 5g**), which overlaps well with the green fluorescence signal from the Alexa Fluor 488-conjugated CD31 antibody (**Fig. 5h, i**). This result suggests the binding of the **RET$_2$IR@cRGD** NPs at the neovascular endothelium of angiogenic tumor blood vessels.

Discussion

While QDs possess excellent optical properties as an imaging probe, concerns such as unfavorable *in vivo* pharmacokinetics after systemic administration, their instability *in vivo*

and intrinsic toxicity due to their formation from toxic heavy metals have limited their use for translational research. In comparison, the self-luminescing NIR NPs show high stability in mouse serum and increased circulation time (**Fig. 2f & g**). Importantly, they do not contain any heavy toxic metals. At a size of around 30-40 nm in diameter, they primarily undergo hepatobiliary clearance in mice, but renal clearance has also been observed (**Fig. 4h & Fig. 5e**). Combined, all these features make the **RET$_2$IR** nanoparticles highly attractive for *in vivo* imaging research.

An important application of fluorescent nanoparticles is lymph node mapping and imaging that traditionally uses vital blue dyes and radioactive tracers in clinics[35]. We have shown highly efficient labeling of all lymph nodes in the lymphatic networks of mice after a single tail-vein injection of **RET$_1$IR** NPs.

Bioluminescence imaging with **RET$_2$IR** NPs gave a tumor-to-background ratio of over 100 and very small subcutaneously implanted tumors (2 or 3 mm in diameter) have been clearly imaged within just 5 mins after the tail-vein injection of the **RET$_2$IR** NPs. This level of sensitivity is at least an order of magnitude higher than fluorescence imaging. With further optimization, tumors smaller than 1 mm in diameter may be readily detectable with the self-luminescing NIR probes.

To the best of our knowledge, our **RET$_2$IR** NP is the first demonstration of a BRET-FRET relay process for *in vivo* imaging. The relay uses a *Renilla* luciferase mutant as the BRET donor, semiconductor polymer MEH-PPV matrix as both the BRET acceptor and the FRET donor, and an NIR dye as the FRET acceptor. The energy transfer relay process was surprisingly efficient. The BRET-FRET relay strategy now allows the use of fluorescent materials other than QDs in building self-luminescing NIR probes for *in vivo* imaging as long as proper fluorophores are chosen to relay the excitation energy from *Renilla* luciferase to the NIR dye dopant, even in multiple relaying steps. Further fine tuning of the probe by matching multiple BRET and FRET pairs should enable self-luminescing NIR NPs for multiplex *in vivo* imaging[21].

Methods

Materials

The poly(phenylene vinylene) derivative poly[2-methoxy-5-(2-ethylhexyloxy)-1,4-phenylenevinylene] (MEH-PPV; MW: 200,000 Da; polydispersity, 4.0) were purchased from ADS Dyes, Inc. (Quebec, Canada). Polystyrene (PS) and polystyrene graft ethylene oxide functionalized with carboxyl groups (PS-PEG-COOH; MW: 21,700 Da of the PS moiety; 1,200 Da of PEG-COOH; polydispersity, 1.25) were purchased from Polymer Source Inc. (Quebec, Canada). Silicon 2,3-naphthalocyanine bis(trihexylsilyloxide) (NIR775) was purchased from Sigma Aldrich, Inc. Cyclic RGD peptide was purchased from Peptides International, Inc. All the other chemicals were purchased from Sigma Aldrich, Inc. and used without purification. Luc8 was prepared according to our previously published procedures[8].

Synthesis of NIR nanoparticles

NIR775-doped NIR nanoparticles were prepared using a nanoscale precipitation technique[30]. In a typical procedure, a solution of tetrahydrofuran (THF) containing 50 μg/mL of MEH-PPV, 50 μg/mL of PS-PEG-COOH, and 0.6 μg/mL of NIR775 dye was prepared. An aliquot of the mixture (5 mL) was then quickly dispersed into 10 mL of water under vigorous sonication. Extra THF was evaporated at an elevated temperature (below 90 °C) under the protection of nitrogen. The THF-free NPs solution was filtrated through a 0.2 μm cellulose membrane filter. Bioconjugation was carried out by the EDC-mediated coupling reaction between the carboxyl groups on the NPs and the amine-containing molecules (Luc8 and RGD peptide). In a typical conjugation reaction, 60 μL of concentrated HEPES buffer (1 M) were added to 3 mL of a solution of the carboxylate-presenting NP (50 μg/mL in water) and the amine-containing molecules (100 μL of Luc8 at 3 mg/mL and 30 μL of RGD peptide at 10 mg/mL), followed by vortex mixing. Then, 50 μL of freshly prepared aqueous EDC solution (10 mg) was added and the above mixture was magnetically stirred for 1 hour at room temperature. The uncoupled free Luc8 and excess EDC were removed by four washes using a 100 K Amicon Ultra filter (Millipore Corporation) under centrifugation at 3,000 rpm for 3 min at 4 °C. The final complex was kept in PBS buffer at 4 °C.

In vitro nanoparticles characterization

The size and morphology of the nanoparticles were investigated using Transmission Electron Microscope (TEM) (FEI Tecnai G2 F20 X-TWIN, 200 kV). TEM samples were prepared by dripping the NP solution onto a carbon-supported copper grid and drying it at room temperature before observation. The hydrodynamic size of the nanoparticles was also measured in aqueous solution by Dynamic Light Scattering (DLS) (Brookhaven 90 Plus Nanoparticle Size Analyzer). The absorption spectra were recorded on an Agilent 8453 UV-Vis spectrometer. Fluorescence and bioluminescence emission spectra were collected with a FluoroMax-3 (Jobin Yvon Inc.) and corrected for wavelength-dependent detector sensitivity as described by the company. In the case of bioluminescence, the excitation light was blocked.

Cell culture, cytotoxicity assay and cell imaging

U87MG (human glioblastoma, high $\alpha_v\beta_3$ expression) cells were grown in DMEM supplemented with 10% FBS. Cultures were maintained at 37 °C under a humidified atmosphere containing 5% CO_2. Cytotoxicity in the U87MG cell line was measured using a methyl thiazolyl tetrazolium (MTT) assay. Cells growing in log phase were seeded into a 96-well cell-culture plate at 1×10^4 cells/well and then incubated for 24 h at 37 °C under 5% CO_2. **RET_1IR** NPs (100 μL/well) were added to the wells of the treatment group at varying concentrations, and 100 μL/well DMEM was added to the negative control group, followed by incubation of the cells for 24 h at 37 °C under 5% CO_2. Subsequently, 10 μL of MTT (5 mg/mL) was added to each well of the 96 well assay plate and incubated for an additional 4 h at 37 °C under 5% CO_2. After the addition of DMSO (200 μL/well), the assay plate was allowed to shake at room temperature for 20 min. A Tecan microplate reader was used to measure the OD_{570} (Absorbance value) of each well with the background subtraction at 690

nm. The following formula was used to calculate the viability of cell growth: cell viability (%) = (mean of Absorbance value of treatment group / mean of Absorbance value of control) × 100.

For cell imaging experiments, 5×10^5 cells per well were seeded on 18 mm glass coverslips and cultured for 24 h before imaging with a Zeiss Axiovert 200M Microscope (excitation: 480/30 nm; dichroic beamsplitter: Q570LP; emission: D755/40M; objective: 20x; acquisition time: 1 s).

Blood circulation half-life in mice

The **RET_1IR** NPs (~20 μg) were injected intravenously into the tail veins of three six-week old nude mice. At various time points postinjection, ~20 μL of blood was collected from the tail into 50 μL of 0.9 % NaCl solution containing 1.5 mg/mL of EDTA. The NIR fluorescence intensity of blood samples was assayed on an IVIS spectrum imaging system (excitation: 465±15 nm; emission: 780±10 nm). Blood samples without the **RET_1IR** NPs were measured to determine the blood autofluorescence level, which was subtracted from the fluorescence intensity of injected samples.

Biodistribution studies

Mice were euthanized by cervical dislocation under deep isoflurane anesthesia. Urine samples were immediately collected, and lymph nodes, brain, spleen, pancreas, kidney, lung, heart, liver, bone (femur), muscle (hind leg), stomach (emptied), and dorsal skin were harvested; for tumor-bearing mice, tumors were also harvested. Tissues were subjected to fluorescence imaging using an IVIS spectrum imaging system immediately (excitation: 465±15 nm; emission: 780±10 nm).

Lymph node imaging

Mice were anesthetized with 2.5% isoflurane, and **RET_1IR** NPs (~20 μg) were administered to nude mice by tail-vein catheterization using the Vevo MicroMarker TVA (Vascular Access) Cannulation Kit (VisualSonics). The tail vein was further flushed with 100 μL of PBS buffer. At 24 h after injection, mice were euthanized, dissected to locate the lymph nodes of interest, and imaged using an IVIS spectrum imaging system immediately (excitation: 465±15 nm; emission: 780±10 nm). Alternatively, ~ 10 μL of **RET_2IR** NPs (~2 μg each) were administered to the forepaws via intradermal injections. Within 10 min of injection, mice received an intravenous injection of 10 μg of coelenterazine for *in vivo* bioluminescence imaging (acquisition time: 10 s; no emission filter). Following bioluminescence imaging, *in vivo* fluorescence imaging was carried out (excitation: 465±15 nm; emission: 780±10 nm).

Tumor implantation and *in vivo* imaging

Animal procedures were approved by the Institutional Animal Care Use Committee of Stanford University. Tumor cells were harvested by incubation with 0.05% trypsin-EDTA when they reached near confluence. Cells were pelleted by centrifugation and resuspended in sterile PBS. U87MG cells (2×10^6 cells/site) were implanted subcutaneously into the left shoulder of four- to five-week-old female nude mice (Charles River Breeding Laboratories).

When the tumors reached the size of 2 to 8 mm in diameter (two to three weeks after implantation), the tumor-bearing mice were subjected to biodistribution and imaging studies. *In vivo* and *ex vivo* fluorescence imaging was performed with an IVIS spectrum imaging system (excitation: 465±15 nm filter; emission: collected from 520 nm to 840 nm with a bandwidth of 20 nm). For bioluminescence imaging, the mice were imaged after tail vein injection of coelenterazine (20 μg/mouse in 20 μL of methanol and 80 μL of phosphate buffer). Images were acquired without filters.

Histology

Tumor-bearing mice were sacrificed 48 h after injection with **RET_2IR@cRGD**. Tumor tissues were collected, washed with PBS, frozen by dry ice and stored at –80 °C. Frozen samples were cryosectioned by microtome at –20 °C into slices of 5 μm thickness, and then fixed in cold acetone for 5 min (–20 °C). Nonspecific binding sites were blocked over 30 minutes with PBS containing 10% mouse serum. The sections were stained with 1 μg of Alexa Fluor 488 anti-mouse CD31 antibody (Biolegend Inc., San Diego, CA) in 100 μL PBS buffer for 1 h at 37 °C. The sections were washed with PBS and analyzed under a Zeiss Axiovert 200M Microscope.

Supplementary Material

Refer to Web version on PubMed Central for supplementary material.

Acknowledgement

We thank Dr. Kai Chen for helpful discussions and suggestions. We acknowledge the use of the SCi^3 Core Facility. This work was supported by the NIH National Cancer Institute (NCI) grants R01CA135294, R21CA138353A2, the Stanford University National Cancer Institute (NCI) CCNE-T grant (U54CA119367) and ICMIC (P50CA114747).

References

1. Ntziachristos V, Ripoll J, Wang LHV, Weissleder R. Looking and listening to light: the evolution of whole-body photonic imaging. Nat. Biotechnol. 2005; 23:313–320. [PubMed: 15765087]
2. McDonald DM, Choyke PL. Imaging of angiogenesis: from microscope to clinic. Nat. Med. 2003; 9:713–725. [PubMed: 12778170]
3. Contag CH, Bachmann MH. Advances in vivo bioluminescence imaging of gene expression. Annu. Rev. Biomed. Eng. 2002; 4:235–260. [PubMed: 12117758]
4. Wagnieres GA, Star WM, Wilson BC. In vivo fluorescence spectroscopy and imaging for oncological applications. Photochem. & Photobiol. 1998; 68:603–632.
5. van Dam GM, et al. Intraoperative tumor-specific fluorescence imaging in ovarian cancer by folate receptor-alpha targeting: first in-human results. Nat. Med. 2011; 17:1315–1319. [PubMed: 21926976]
6. Frangioni JV. In vivo near-infrared fluorescence imaging. Curr. Opin. Chem. Biol. 2003; 5:626–634. [PubMed: 14580568]
7. So M-K, Xu C, Loening AM, Gambhir SS, Rao J. Self-illuminating quantum dot conjugates for in vivo imaging. Nat. Biotechnol. 2006; 24:339–343. [PubMed: 16501578]
8. So M-K, Loening AM, Gambhir SS, Rao J. Creating self-illuminating quantum dot conjugates. Nat. Protocols. 2006; 1:1160–1164. [PubMed: 17406398]
9. Wu C, Kawasaki K, Ohgiya S, Ohmiya Y. Chemical studies on the BRET system between the bioluminescence of Cypridina and quantum dots. Photochem. Photobiol. Sci.

10. Du J, et al. Quantum-dot-decorated robust transductable bioluminescent nanocapsules. J. Am. Chem. Soc. 2010; 132:12780–12781. [PubMed: 20795619]
11. Bacart J, Corbel C, Jockers R, Bach S, Couturier C. The BRET technology and its application to screening assays. Biotechnol. J. 2008; 3:311–324. [PubMed: 18228541]
12. Yao H, Zhang Y, Xiao F, Xia Z, Rao J. Quantum dot/bioluminescence resonance energy transfer based highly sensitive detection of proteases. Angew. Chem. Int. Ed. 2007; 46:4346–4349.
13. Xia Z, et al. Multiplex detection of protease activity with quantum dot nanosensors prepared by intein-mediated specific bioconjugation. Anal. Chem. 2008; 80:8649–8655. [PubMed: 18922019]
14. Cissell KA, Campbell S, Deo SK. Rapid, single-step nucleic acid detection. Anal. Bioanal. Chem. 2008; 391:2577–2581. [PubMed: 18563395]
15. Kosakaa N, et al. Self-illuminating in vivo lymphatic imaging using a bioluminescence resonance energy transfer quantum dot nano-particle. Contrast Media Mol. Imaging. 2011; 6:55–59. [PubMed: 21351373]
16. Xing Y, So M-K, Koh AL, Sinclair R, Rao J. Improved QD-BRET conjugates for detection and imaging. Biochem. Biophy. Res. Comm. 2008; 372:388–394.
17. Schipper ML, et al. Particle size, surface coating, and PEGylation influence the biodistribution of quantum dots in living mice. Small. 2009; 5:126–134. [PubMed: 19051182]
18. Schipper ML, et al. MicroPET-based biodistribution of quantum dots in living mice. J. Nucl. Med. 2007; 48:1511–1518. [PubMed: 17704240]
19. Pecher J, Mecking S. Nanoparticles of conjugated polymers. Chem. Rev. 2010; 110:6260–6279. [PubMed: 20684570]
20. Rahim NAA, et al. Conjugated polymer nanoparticles for two-photon imaging of endothelial cells in a tissue model. Adv. Mater. 2009; 21:3492–3496.
21. Wu C, Bull B, Szymanski C, K. Christensen K, McNeill J. Multicolor conjugated polymer dots for biological fluorescence imaging. ACS Nano. 2008; 2:2415–2423. [PubMed: 19206410]
22. Pu KY, Li K, Shi JB, Liu B. Fluorescent single-molecular core−shell nanospheres of hyperbranched conjugated polyelectrolyte for live-cell imaging. Chem. Mater. 2009; 21:3816–3822.
23. Tang H, Xing C, Liu L, Yang Q, Wang S. Synthesis of amphiphilic polythiophene for cell imaging and monitoring the cellular distribution of a cisplatin anticancer drug. Small. 2011; 7:1464–1470. [PubMed: 21506263]
24. Wu C, et al. Bioconjugation of ultrabright semiconducting polymer dots for specific cellular targeting. J. Am. Chem. Soc. 2010; 132:15410–15417. [PubMed: 20929226]
25. Loening AM, Fenn TD, Wu AM, Gambhir SS. Consensus guided mutagenesis of Renilla luciferase yields enhanced stability and light output. Protein Eng. Des. Sel. 2006; 19:391–400. [PubMed: 16857694]
26. Ruoslahti E. RGD and other recognition sequences for integrins. Annu. Rev. Cell Dev. Biol. 1996; 12:697–715. [PubMed: 8970741]
27. Hood JD, Cheresh DA. Role of integrins in cell invasion and migration. Nat. Rev. Cancer. 2002; 2:91–100. [PubMed: 12635172]
28. Xiong JP, et al. Crystal structure of the extracellular segment of integrin $\alpha_V\beta_3$ in complex with an Arg-Gly-Asp ligand. Science. 2002; 296:151–155. [PubMed: 11884718]
29. Ye Y, Bloch S, Xu B, Achilefu S. Design, synthesis, and evaluation of near infrared fluorescent multimeric RGD peptides for targeting tumors. J. Med. Chem. 2006; 49:2268–2275. [PubMed: 16570923]
30. Jin YH, Ye FM, Zeigler M, Wu CF, Chiu DT. Near-infrared fluorescent dye-doped semiconducting polymer dots. ACS Nano. 2011; 5:1468–1475. [PubMed: 21280613]
31. Kim S, et al. Near-infrared fluorescent type II quantum dots for sentinel lymph node mapping. Nat. Biotechnol. 2004; 22:93–97. [PubMed: 14661026]
32. Kobayashi H, et al. Simultaneous multicolor imaging of five different lymphatic basins using quantum dots. Nano Lett. 2007; 7:1711–1716. [PubMed: 17530812]
33. Kim S, et al. Conjugated polymer nanoparticles for biomedical in vivo imaging. Chem. Comm. 2010; 46:1617–1619. [PubMed: 20177593]

34. Harisinghani MG, et al. Noninvasive detection of clinically occult lymph-node metastases in prostate cancer. New Eng. J. Med. 2003; 348:2491–2499. [PubMed: 12815134]

35. Tanaka E, et al. Image-guided oncologic surgery using invisible light: completed pre-clinical development for sentinel lymph node mapping. Ann. Surg. Oncol. 2006; 13:1671–1681. [PubMed: 17009138]

36. Ballou B, et al. Noninvasive imaging of quantum dots in mice. Bioconjugate Chem. 2004; 15:79–86.

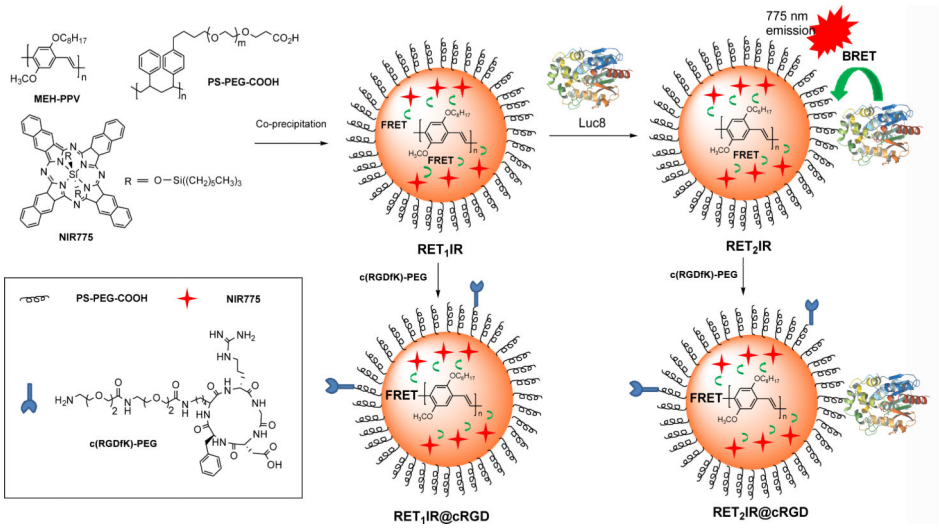

Figure 1.

Schematic of self-luminescing BRET-FRET near infrared (NIR) polymer nanoparticles. The biochemical energy generated from the Luc8-catalyzed oxidation of coelenterazine transfers initially to the MEH-PPV polymer and is then relayed to doped NIR775 dye to produce NIR emission. An amphiphilic polymer, PS-PEG-COOH, coats the nanoparticle to improve water solubility and biocompatibility. Tumor targeting ligands such as cyclic RGD peptides are conjugated to the nanoparticle surface for *in vivo* cancer imaging.

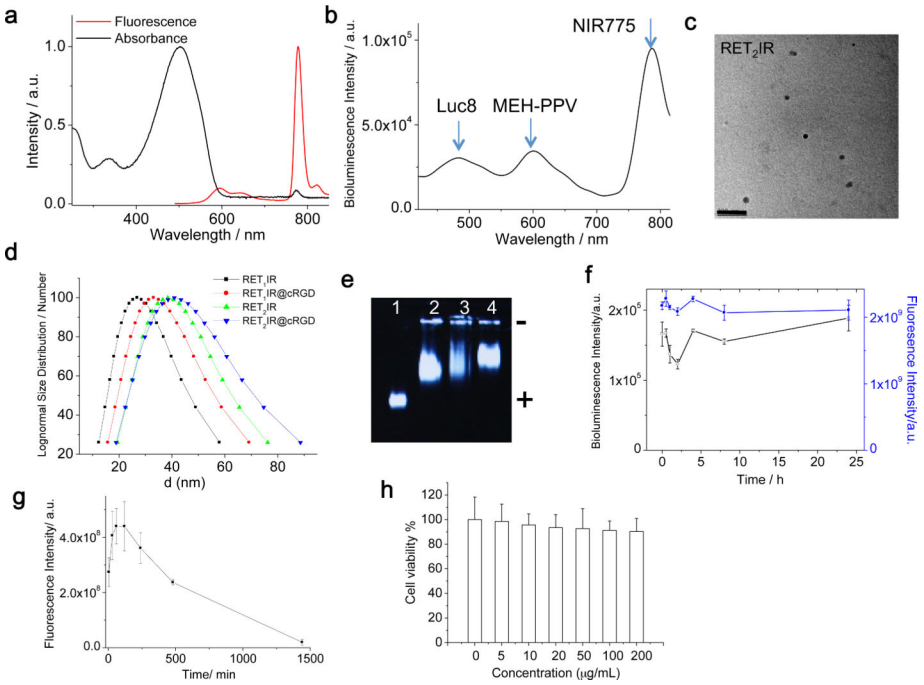

Figure 2.

In vitro characterization of RET IR nanoparticles. (**a**) UV-Vis absorption and fluorescence emission spectra of **RET_2IR** NPs in PBS buffer. (**b**) Bioluminescence emission spectrum of **RET_2IR** NPs in PBS buffer. (**c**) Representative transmission electron microscopy (TEM) image of **RET_2IR** NPs. Scale bar = 200 nm. (**d**) Dynamic light scattering (DLS) measurement of four indicated NP formulations in water by lognormal size distribution. (**e**) Gel electrophoresis (0.5% agarose) analysis of RET NPs in tris-borate-EDTA (TBE) buffer: **RET_1IR** (lane 1), **RET_1IR@cRGD** (lane 2), **RET_2IR** (lane 3), **RET_2IR@cRGD** (lane 4). (**f**) Bioluminescent and NIR fluorescent intensity of **RET_2IR** NPs (1 μg) in mouse serum at 37°C from 0 h to 24 h. Data points represent mean±s.d. (n=3). (**g**) The NIR fluorescence signals of blood samples of mice injected with **RET_1IR** NPs (~20 μg) from 5 min to 24 h. Data represent mean±s.d. (n=4). (**h**) Viability values (%) of U87MG cells estimated by MTT assay versus incubation concentrations of **RET_1IR** NPs. Data represent mean+s.d. (n=3).

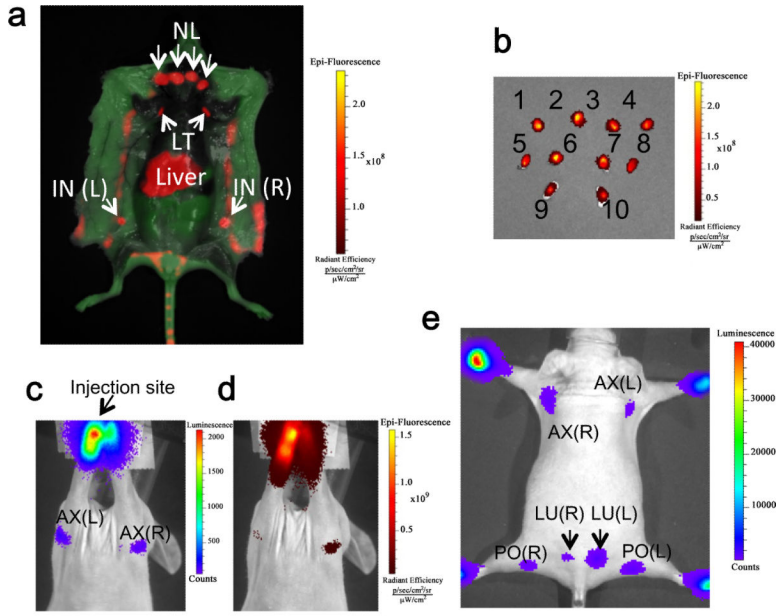

Figure 3.

Fluorescence and bioluminescence imaging of lymph nodes in mice. (**a**) Fluorescence imaging of a mouse following sacrifice and necropsy 24 h after the tail-vein injection of **RET$_1$IR** NPs (~20 μg). Superficial skin was removed before imaging but peritoneum was left intact. Autofluorescence is coded in green and NPs signal in red; NL, neck lymph nodes; AX, axillary lymph node; LT, lateral thoracic lymph node; IN, inguinal lymph node; L, left; R, right. (**b**) Fluorescence image of lymph nodes excised from the mouse in (**a**): 1-4, NL; 5, AX (Left); 6, LT (Left); 7, LT (Right); 8, AX (Right); 9, IN (Left), 10 IN (Right). (**c**) Bioluminescence and (**d**) fluorescence imaging of lymphatic basins in a mouse 10 mins after the injection of **RET$_2$IR** NPs (~2 μg) intradermally in the forepaws. (**e**) Bioluminescence imaging of lymphatic basins in a mouse with injection of **RET$_2$IR** NPs (~2 μg) intradermally in the forepaws. All bioluminescence images were acquired with 10 s exposure time; PO, popliteal lymph node; LU, lumbar lymph node; L, left; R, right.

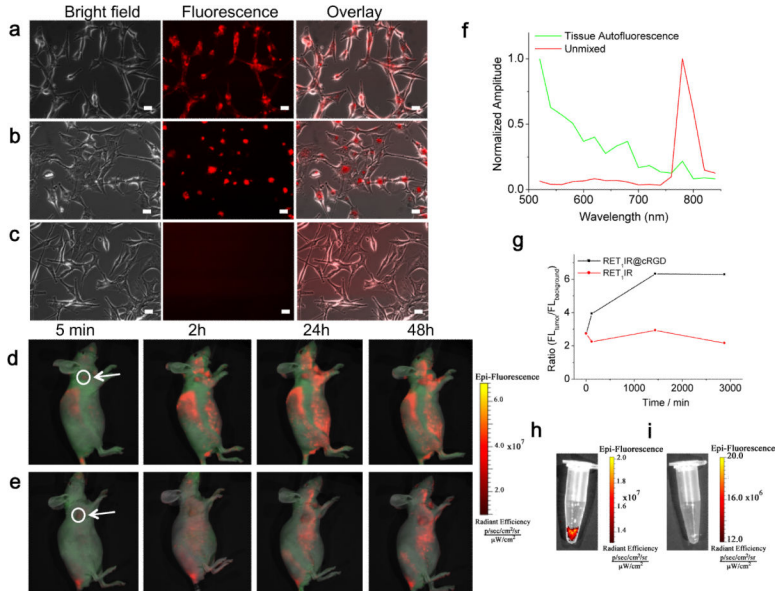

Figure 4.

Fluorescence imaging of U87MG cells *in vitro* and *in vivo* with **RET$_1$IR@cRGD** NPs. (**a-c**) Live imaging of U87MG cells *in vitro* incubated with **RET$_1$IR@cRGD** NPs (4 μg) for (**a**) 2.5 h and (**b**) 24 h, or (**c**) incubated with **RET$_1$IR** NPs without cRGD for 24 h. Scale bar: 20 μm; excitation: 480/30 nm, dichroic beamsplitter: Q570LP, emission: D755/40M; objective: 20x; acquisition time: 1 s. (**d, e**) Time-dependent fluorescence imaging of U87MG tumor-bearing mouse (tumors are indicated by white arrows and circles, and are 4 mm in diameter) injected with (**d**) **RET$_1$IR@cRGD** or (**e**) **RET$_1$IR** NPs (each at ~50 μg) after 5 min, 2 h, 24 h and 48 h. Autofluorescence is coded in green and the unmixed polymer nanoparticle signal in red. (**f**) Fluorescence spectra of tissue autofluorescence (green) and the unmixed nanoparticle signal (red) in a living mouse. (**g**) ROI analysis of fluorescence intensity of tumor over background of mice in (**d**) and (**e**). Using one-tailed paired Student's t-test (n = 3 mice injected with **RET$_1$IR@cRGD**), $p < 0.05$ at 24 h. (**h, i**) NIR fluorescence imaging of urine samples (**h**) collected 48 h after injection from mouse in (**d**), and (**i**) from a mouse without any nanoparticle injection.

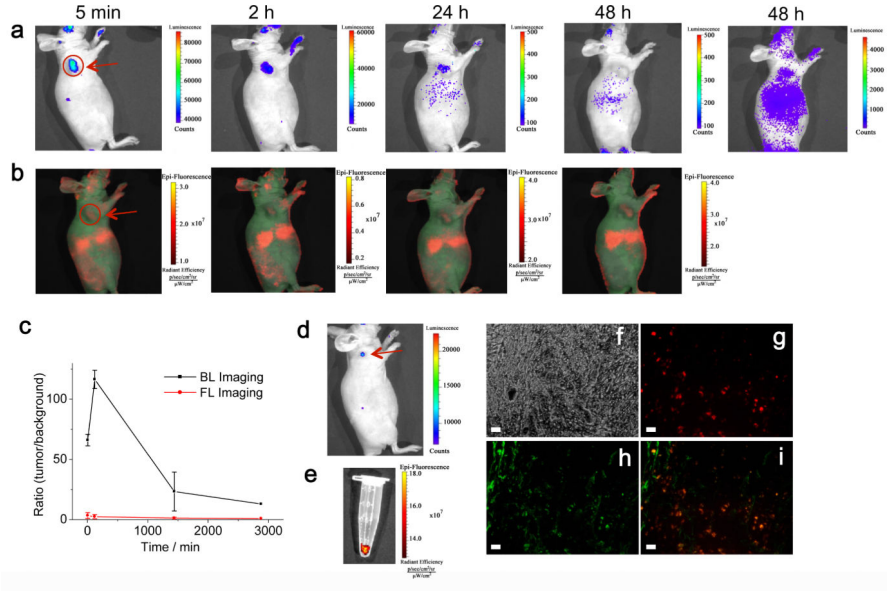

Figure 5.

In vivo imaging of U87MG tumors in mice with **RET$_2$IR@cRGD**. (**a, b**) Time-dependent (**a**) *in vivo* bioluminescence and (**b**) fluorescence imaging of U87MG tumor-bearing mouse (indicated by a red arrow and circle; tumor size was about 5 mm in diameter) injected with **RET$_2$IR@cRGD** NPs (~50 μg). Acquisition time for images in (**a**) from left to right: 15 s (5 min), 15 s (2 h), 1 min (24 h), 1 min (48 h), and 3 min (48 h). (**c**) ROI analysis of the bioluminescence and fluorescence intensity between tumor and background of mice in (**a**) and (**b**). Using one-tailed paired Student's t-test (n = 3), $p < 0.00002$ at 5 min, and 2 h, $p < 0.04$ at 24 h, and $p > 0.05$ at 48 h. (**d**) *In vivo* bioluminescence imaging of a mouse with a small tumor of 2 mm in diameter, as indicated by a red arrow, 2 h after tail vein injection of **RET$_2$IR@cRGD**. (**e**) NIR fluorescence imaging of urine samples collected 48 h after injection from mice in (**a**). Data points represent mean±s.d. (n=4) (**f-i**) Histological imaging of frozen U87MG tumor slices from mouse in (**a**): (**f**) bright field, (**g**) NIR fluorescence (excitation filter: 480/30 nm, dichroic beamsplitter: Q570LP, emission filter: D755/40M, acquisition: 1 s), (**h**) Alexa Fluor 488 anti-mouse CD31 (excitation: 480/30 nm, dichroic beamsplitter: 505DCLP, emission: D535/40 nm, acquisition time: 200 ms), and (**i**) overlay of images in (**g**) and (**h**). Scale bar: 20 μm, objective: 20x.